Journal of Instrumentation

Construction and test of a small-pad resistive Micromegas prototype

Published by IOP Publishing for Sissa Medialab

Received: *August 19, 2018*
Accepted: *November 5, 2018*
Published: *November 23, 2018*

Construction and test of a small-pad resistive Micromegas prototype

M. Alviggi,[a,b] **V. Canale,**[a,b] **M. Della Pietra,**[a,b] **R. De Oliveira,**[c] **C. Di Donato,**[d,b,] **E. Farina,**[e] **S. Franchino,**[f] **P. Iengo,**[c] **M. Iodice,**[g] **F. Petrucci,**[h,g,1] **E. Rossi,**[h,g] **G. Sekhniaidze,**[b] **O. Sidiropoulou**[c] **and V. Vecchio**[h,g]

[a] *Università di Napoli Federico II,*
Strada Comunale Cintia, 80126 Naples, Italy
[b] *INFN Napoli,*
Strada Comunale Cintia, 80126 Naples, Italy
[c] *European Center for Nuclear Research, CERN,*
Route de Meyrin 385, 1217 Meyrin, Switzerland
[d] *Università di Napoli "Parthenope",*
Via Ammiraglio Ferdinando Acton 38, 80133 Naples, Italy
[e] *Università di Pavia and INFN Pavia,*
Via A. Bassi 6, 27100 Pavia, Italy
[f] *Ruprecht-Karls-Universität Heidelberg - Kirchhoff-Institut für Physik (KIP)*
Im Neuenheimer Feld 227, 69120 Heidelberg, Germany
[g] *INFN Roma Tre,*
Via della Vasca Navale 84, 00146 Rome, Italy
[h] *Università Roma Tre,*
Via della Vasca Navale 84, 00146 Rome, Italy

E-mail: fabrizio.petrucci@cern.ch

Abstract: Resistive Micromegas are nowadays a mature technology for High Energy Physics experiments. In the ATLAS experiment at CERN these detectors will operate at hit rates up to 15 kHz/cm^2. Future upgrades of existing experiments and new detectors at future accelerators will require operation at rates up to three orders of magnitude higher. In this paper we present the design, construction and test of a Micromegas with a pad resistive readout of few mm^2 in size. We aim at precision tracking in high rate environment without efficiency loss up to tens of MHz/cm^2. The detector layout and the construction technique are described, along with a characterisation of its performance, carried out by means of radioactive sources, X-rays and high energy particle beams.

Keywords: Gaseous detectors; Micropattern gaseous detectors (MSGC, GEM, THGEM, RETHGEM, MHSP, MICROPIC, MICROMEGAS, InGrid, etc); Particle tracking detectors (Gaseous detectors)

[1] Corresponding author.

https://doi.org/10.1088/1748-0221/13/11/P11019

2018 JINST 13 P11019

Contents

2018 JINST 13 P11019

1 Introduction

Developed in the '90s [1], Micromegas detectors are based on a double gas gap structure: conversion (or drift) and amplification regions, where ionization and avalanche multiplication take place, respectively. The drift region is generally few mm wide and is separated from the amplification region by a planar mesh electrode, kept at order of hundred microns with respect to the anode plane through a pillars matrix. First resistive [2] Micromegas detectors were developed with a strip readout plane in view of the ATLAS New Small Wheel (NSW) muon spectrometer upgrade [3], where high tracking efficiency is needed in a high background environment. The term 'resistive' refers to the presence of a resistive plane of strips on the top of the readout plane, with a kapton foil as insulator in between. This solution reduces the discharge intensity, quenched by the resistive layer, and the associated damages without spreading too much the avalanche footprint; high efficiencies ($> 98\%$) are achieved for rates up to 15 kHz/cm^2. In order to further increase the rate capability, up to tens of MHz/cm^2, a further re-arrangement is introduced, where the resistive and read-out planes are changed to small pads (O (mm^2)), lowering the detector occupancy. The proposed detector is inspired by a similar development considered for the COMPASS experiment [4] and sampling calorimetry [5] and based on a solution proposed in 2010 [6]. The idea is to have the readout pads overlaid by resistive pads, both interconnected by intermediate resistors embedded in the structure. In these schema the signal is read from the copper pads and the charges are evacuated through the

intermediate resistors. In the next section more details on the prototype construction are presented. Then, in section 3 the detector characterization carried out by means of radioactive sources is extensively described. Detector performances, as efficiency and space resolution, measured with high energy muon beam, are reported in section 4. Finally, in section 5 the performances under high flux of radiation are shown. The work presented here is the result of a study started in 2016; preliminary results on some of the topics have already been shown at conferences ([7, 8]).

2 Small-pad Resistive Micromegas construction details

The schematic concept of the first small-pad Micromegas (pad-MM) detector prototype built at CERN in 2016 [7] is shown in figure 1. The copper readout plane is segmented in $0.8 \times 2.8\,\mathrm{mm}^2$ dimension pads with a pitch of 1 and 3 mm, forming a matrix with 48 pads along the precise coordinate (that will be referred as x direction in the text) and 16 pads along the orthogonal direction (y direction). In total 768 readout channels are present, for a total active area of $48 \times 48\,\mathrm{mm}^2$.

The resistive protection is obtained with two patterned layers of carbon paste resistors, having the same size of the readout pads, separated by 12.5 μm thick Kapton foils (embedded resistors). The production follows few steps: a first layer of kapton foil is glued onto the readout board with etched copper pads. Then pad-shaped resistors are screen printed on the kapton and the electrical connection with the readout pads is done with micro-vias in the kapton filled with silver paste. A second foil of kapton is then stacked and glued, with vias again filled with silver paste. The vias on the two layers are staggered: in this way the electron current evacuated through the readout pads is always made to flow through at least one full embedded resistor. A coverlay is laminated on top defining rectangular enclosures of the same size of the readout pads, filled with resistive paste and polished with sand paper grade 1000 to 2500 to guarantee the flatness. For a large fraction of the pads the resistance has been measured between the resistive and the copper pads, obtaining values ranging from 3 to 7 MΩ. Such values have been chosen as a trade-off between a high spark protection of the resistive layer and a good detector's rate capability.

The detector is completed with a bulk-Micromegas process [9], defining the ∼ 100 μm amplification gap with a stainless steel micro-mesh of 400 lines per inch, made of woven wires with a diameter of 18 μm. The mesh is supported by small pillars (400 mm diameter) made of Pyralux and placed at 2.5 mm from each other in both directions.

The detector is finally closed assembling a cathode plane (a 50 μm thin copper clad kapton foil) at 5 mm distance from the mesh, defining the conversion and drift gap.

A different approach for the resistive layer was used in the construction of a previous prototype with the same readout segmentation. It was based on full screen printing of all layers (including the embedded resistor and the insulation layer) on top of the copper based anode board. This technique had several advantages. It was simple, cost effective and easy to scale to a larger size. Unfortunately, the detector suffered from high voltage instabilities, and several attempts of reparation were not successful. The problem was possibly caused by the bad quality of the screen-printed insulation layer, between the anode and the top resistive pads, developing pin-holes and causing discharges. Therefore, such an approach has not been pursued nor developed further. However its simplicity and cost advantages could be good reasons to reconsider it for large productions.

2018 JINST 13 P11019

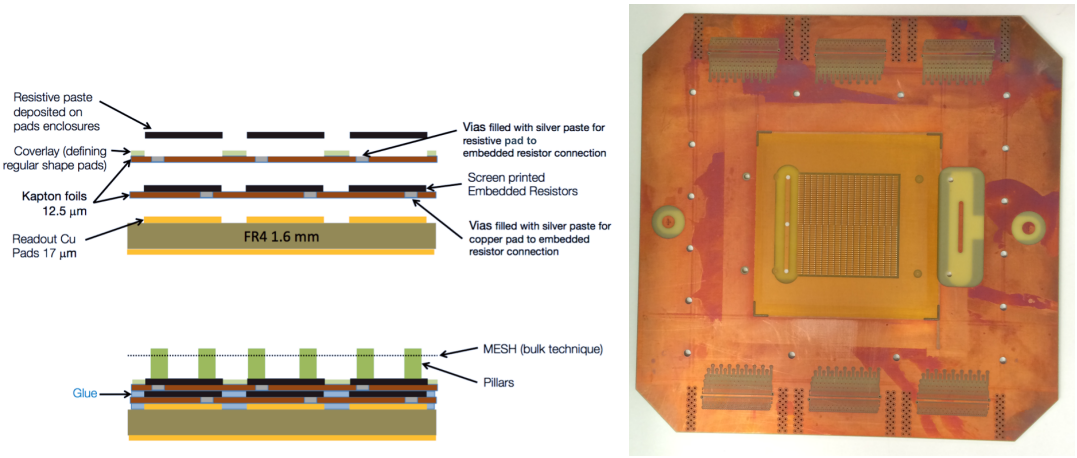

Figure 1. Left: schematic view of the detector. Right: picture of detector anode.

3 Detector characterisation

The pad-MM prototype has been extensively tested in the GDD (Gas Detector Development) laboratory of the RD51 [10] Collaboration at CERN, using different radiation sources and measuring its performances in different conditions. All the measurements have been carried out using a gas mixture with Argon and CO_2 at 93% and 7% respectively. The detector has been operated with the readout pads connected to ground through the preamplifier input impedence. Negative voltages were applied to the mesh (V_{amp}) and to the cathode plane ($V_{cathode}$); V_{amp} defines the electric field in the amplification region while $V_{drift} = V_{cathode} - V_{amp}$ defines the drift electric field. Typical values are $V_{amp} \sim 500$ V and $V_{drift} \sim 300$ V. In the following, all the voltages applied to the electrodes have to be considered as negative values if not stated otherwise.

Gain and electron transparency have been measured exposing the detector to two ^{55}Fe sources with different activities: the first one corresponding to a measured rate of 1.3 kHz ("Low activity source") and the second one corresponding to a rate of 128 kHz ("High activity source"). The uniformity of the detector response has also been measured by irradiating small portions of the detector surface at a time. Some tests have been repeated at different times showing a good stability of the detector performance.

The experimental setup is described in figure 2-left. The detector current is measured with a high resolution picoammeter collecting the current from all the readout pads. Signals collected on the mesh go first to a charge amplifier stage and then to both a scaler and a Multi-Channel Analyzer (MCA).

Figure 3-left shows the energy spectra obtained with the "Low" activity ^{55}Fe source, measured through the MCA for two different detector amplification voltages, 520 V or 530 V, applied to the mesh; the drift voltage was constantly kept 200 V higher than the mesh voltage. We measured an energy resolution, defined as the ratio between FWHM and peak value, of about 40%.

There are two main contribution to the modest energy resolution:

- the distortion of the electric field due to pad border effects;
- a non-flat and uniform deposition of the embedded resistors.

2018 JINST 13 P11019

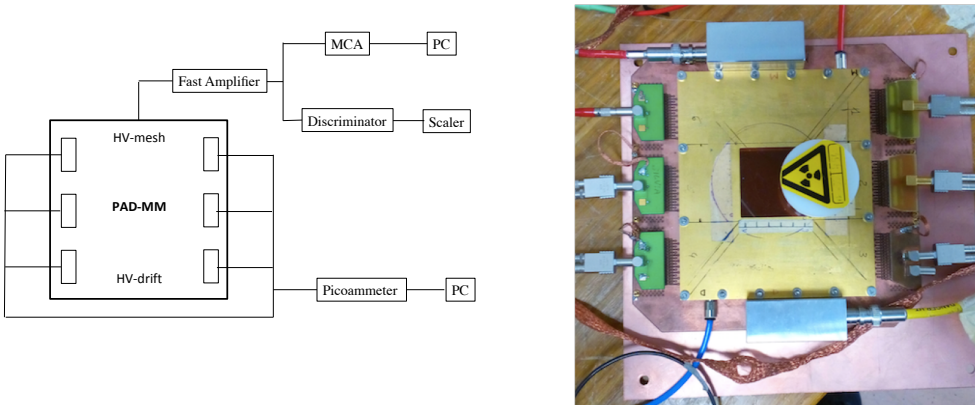

Figure 2. Left: schema of current and rate measurements: detector current is measured from anode pads connectors through an high resolution picoammeter; signals from the mesh are amplified and then counted with a scaler and analyzed with a MCA. Right: picture of the experimental setup during ^{55}Fe irradiation.

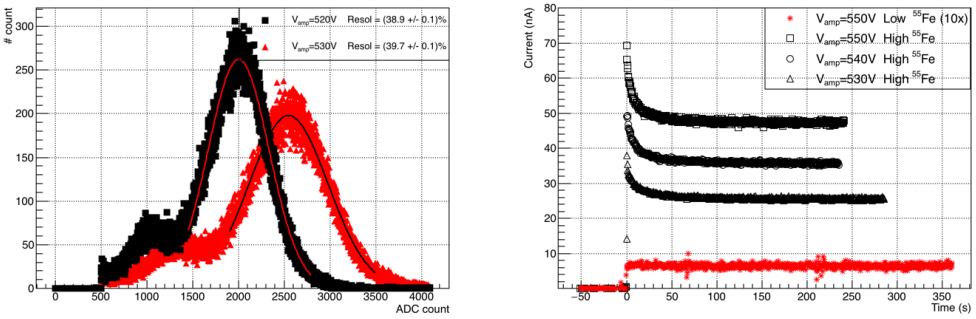

Figure 3. Left: energy spectra for "Low" activity ^{55}Fe source. Right: detector current as a function of time for different amplification voltages and different activities of the ^{55}Fe source; with the "Low" activity source the detector current has been magnified by a factor ten.

The latter can provide locally (for each pad) a different capacitive coupling to the readout pads, depending on where the avalanche occurs.

Figure 3-right shows the evolution of the current as a function of the time under "High" activity ^{55}Fe source irradiation for three different detector amplification voltages (530 V, 540 V and 550 V); a reduction with time of about 30% after 100 seconds is clearly visible. This effect has been interpreted as owing to charging-up of the dielectric that surrounds the resistive pads, causing a local reduction of the amplification field. On the same plot, the current measured with the "Low" activity ^{55}Fe source for a detector amplification voltage of 550 V, magnified by a factor ten, is also reported; no drop is observed in the same time scale.

The detector gain, defined as the ratio between the collected charge and the expected average number of electrons produced by the ionizing radiation in the conversion region, has been measured in different periods, using both ^{55}Fe sources, as a function of the amplification voltage: results are shown in figure 4-left. Two different methods have been used to measure the collected charge

2018 JINST 13 P11019

for each ^{55}Fe photon conversion: from the Auger peak position in the MCA spectrum and from the detector current and rate measured in the detector. The gain curves corresponding to the Low activity ^{55}Fe source, measured with the two methods and at different times, are compatible with each other. The curve measured with the High activity ^{55}Fe source shows a lower gain of about 25%. This measurement is in agreement with the current reduction shown in figure 3-right.

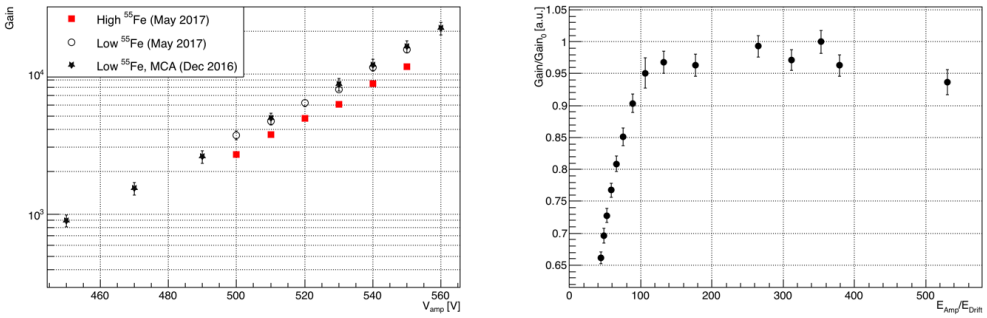

Figure 4. Left: gain as a function of amplification voltage for different ^{55}Fe sources and different periods in logarithmic scale. For all the curves the gain has been measured from the detector current, except for the one measured with the MCA (star markers). Right: relative mesh transparency as a function of amplification and drift electric field ratio. Reproduced with permission from [8].

The gain has been measured also as a function of the drift voltage, keeping the amplification voltage constant; the relative mesh transparency to electrons as a function of amplification and drift electric fields ratio is then defined as the ratio of the measured gain with respect to its maximum over the explored interval (Gain0). As reported in figure 4-right the relative transparency reaches a plateau for electric fields ratio approximately between 100 and 400 for an amplification voltage of 530 V. The drop at larger values of the electric fields ratio is due to recombinations occurring at very low drift voltage values.

4 Test Beam results

4.1 Experimental setup

The pad-MM prototype was exposed to high energy muon and pion beams at the CERN SPS H4 beam line in October 2016.

The experimental setup consisted of the pad-MM and of two 10x10 cm^2 resistive-strips bulk Micromegas (Tmm chambers) with a double coordinate readout, used as reference tracking chambers. The three detectors were placed on an aluminum support structure with the Tmm chambers at a distance of about 50 mm from the pad-MM, one before and one after the pad-MM along the beam line. Two 100×100 mm^2 scintillators, placed before and after Tmm chambers, were used as a beam trigger. The active area of the trigger scintillators and of the Tmm chambers was larger than the 48×48 mm^2 of the pad-MM detector. Only 2/3 of the strips of the Tmm chambers was read-out in both coordinates resulting in an active area of about 60×60 mm^2. The detector positions were adjusted to have the available trigger and tracking area centred to cover the full pad-MM surface. The Ar/CO_2 93-7 gas mixture was distributed in series to all the detectors.

2018 JINST 13 P11019

The system was readout using the RD51 SRS system [11] connected to hybrid front-end read-out boards equipped with APV25 chips [12].

A reference system has been defined with the z axis directed as the incoming beam particles, the y axis pointing to the ground and the x axis parallel to the ground. We are naming the x and y coordinates of the Tmm chambers and of the pad-MM accordingly to this definition. The precision coordinate (with 1 mm pitch) of the pad-MM is then the x-coordinate while the second coordinate (with 3 mm pitch) is the y-coordinate.

Data were collected with the Tmm reference chambers at a fixed operating point while changing the applied voltages of the pad-MM. The amplification voltage was varied from 440 V to 540 V while the drift voltage was kept fixed at 300 V.

The experimental setup was the same in both the muon and pion beam cases.

In this section results obtained with the muon beam are reported, while the measurements with the pion beam are discussed in section 5.

An event (i.e. a trigger from the coincidence of the two scintillators) was considered for the successive analysis if one and only one cluster of adjacent strips was reconstructed in both views in each one of the Tmm tracking chambers. This was required to have a clean reference track sample, considering that our reference tracking system was only made by the two Tmm chambers. The fraction of good events ranges from 40% to 60% of the total, depending on the run and beam conditions. It has to be noted that $\sim$ 35% of the recorded events are discarded because the trigger area is larger than the instrumented area of the Tmm chambers.

From the clusters in both views of the Tmm chambers a reference track is fit and interpolated to the position of the pad-MM to measure resolution and efficiency. Detectors positions and relative rotations were corrected offline with an iterative procedure looking at the distribution of the track residuals as a function of the x and y coordinates. Considering a spatial resolution of 70 µm for each Tmm chamber, as measured in previous studies, an interpolation error of $\sim$ 50 µm is obtained on the pad-MM detector position.

4.2 Detector performance

4.2.1 Cluster multiplicity, size and charge

Pads charge and multiplicities distributions were studied first. To suppress the noise, a cut on the pads charge was imposed. It was set, separately for each channel, at five times the RMS of the distribution of the ADC pedestal. The latter were extracted from dedicated runs taken with a random trigger. The distribution of the pads charge is shown as an example in figure 5-left for two different runs with an amplification voltage of 480 V and 500 V respectively. In the insert, a zoomed view of the distribution at low values is shown.

The distribution shows a saturation peak (due to the APV25 dynamical range) around 1800 ADC counts. As expected, the saturation is more evident in the run at larger amplification voltage where the collected charge is larger. The distribution of the applied charge threshold for each channel is shown in figure 5-right.

Clusters within the pad-MM are reconstructed combining adjacent fired pads. The cluster position is given by the charge weighted average of the pads positions (charge centroid). The distribution of the cluster charge is shown in figure 6 for three different runs with an amplification

2018 JINST 13 P11019

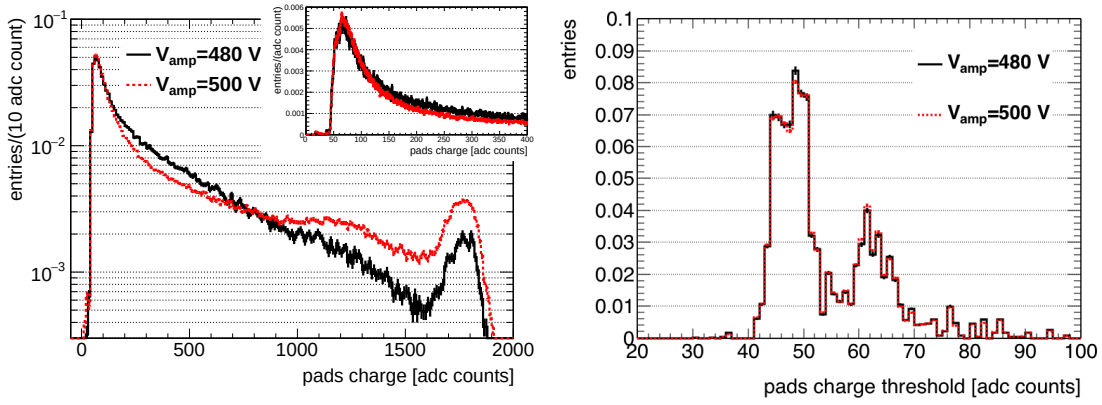

Figure 5. Left: pads charge distribution in two different runs with V_{amp} = 480 V and V_{amp} = 500 V (the insert plot shows, with a smaller bin size on the x axis, a zoom to the initial part of the distribution). Right: distribution of the charge threshold ($5 \times \sigma_{ped}$) for each pad.

voltage of 460 V, 480 V and 490 V. A fit with a Landau distribution is shown as a superimposed dotted line. As expected, the cluster charge increases with the amplification voltage. At larger amplification voltages, the cluster charge distribution starts to be distorted; this is mainly due to the saturation effect of the electronics response, as already pointed out for the charge distribution of the single pads.

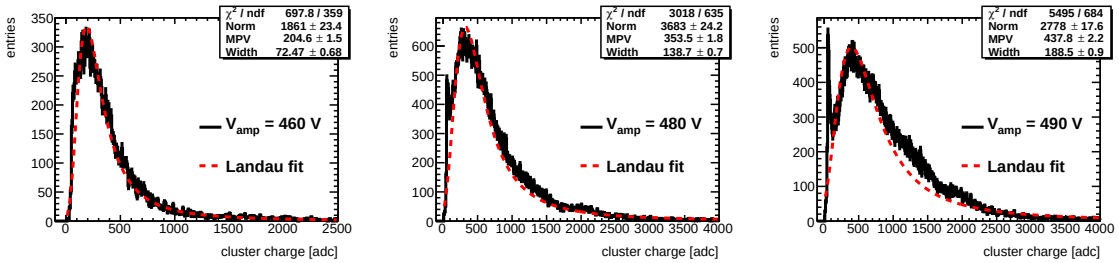

Figure 6. Cluster charge distribution in tree different runs with V_{amp} equals to 460 V, 480 V and 490 V respectively. A fit with a Landau distribution is shown as a superimposed dotted line.

In figure 7-left the distribution of the number of reconstructed clusters per event is shown for two different runs with V_{amp} = 480 V and V_{amp} = 500 V (the insert plot shows the same distributions in a logarithmic vertical scale) while in figure 7-right the mean number of reconstructed clusters per event is reported as a function of the applied amplification voltage. We observe an increase in the number of clusters per event at very high amplification voltage due to noise hits.

The distribution of the number of pads per cluster is shown in figure 8-left for two different runs with V_{amp} = 480 V and V_{amp} = 500 V (the insert plot shows the same distributions in a logarithmic vertical scale). As can be observed from figure 8-right, the mean number of pads per cluster ranges from ~ 1 up to 3 at large amplification voltage. This has an impact on the precision of the measurement of the cluster position (based on the charge centroid) and thus on the resolution (as shown in the next section).

The number of fired pads in a cluster depends also on the position of the particle track with respect to a pad. In figure 9, the fraction of events with an odd (left) or even (right) number of pads

2018 JINST 13 P11019

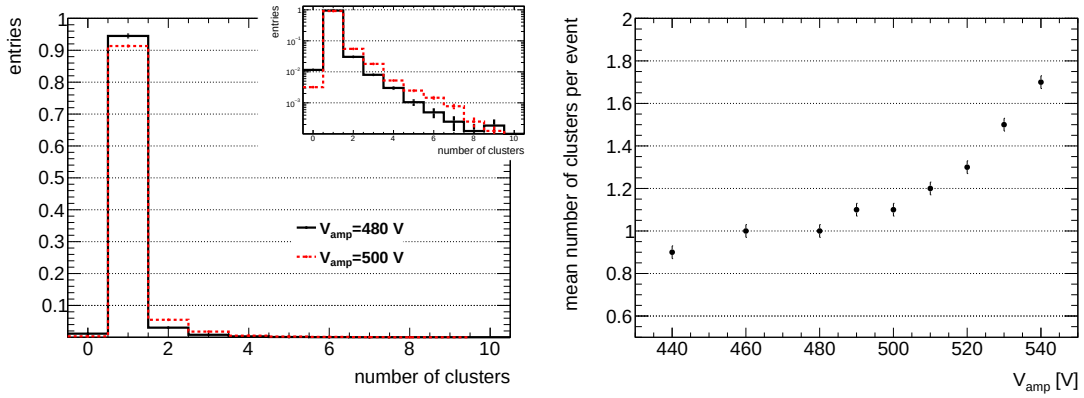

Figure 7. Left: distribution of the number of clusters per event in two different runs with V_{amp} = 480 V and V_{amp} = 500 V (the insert plot shows the same distributions in a logarithmic vertical scale). Right: mean number of reconstructed clusters per event as a function of the applied amplification voltage.

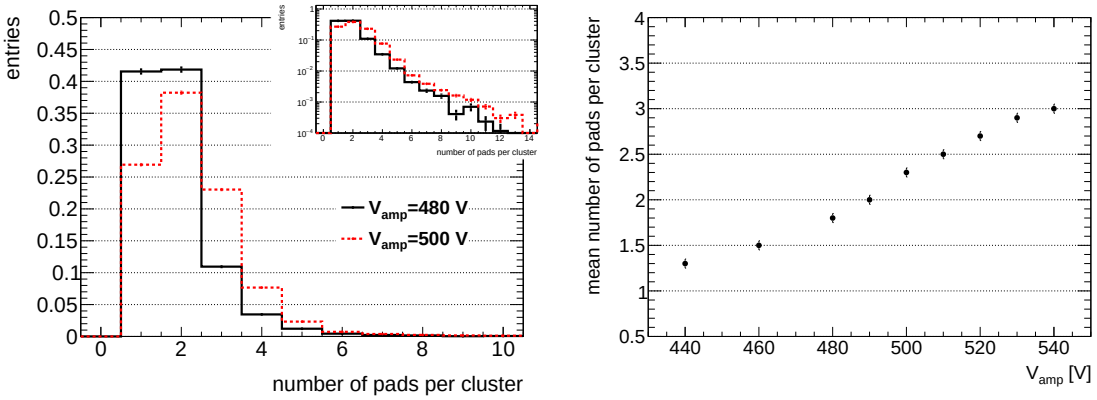

Figure 8. Left: distribution of the number of pads per cluster in two different runs with V_{amp} = 480 V and V_{amp} = 500 V (the insert plot shows the same distributions in a logarithmic vertical scale). Right: mean number of pads per cluster as a function of the applied amplification voltage.

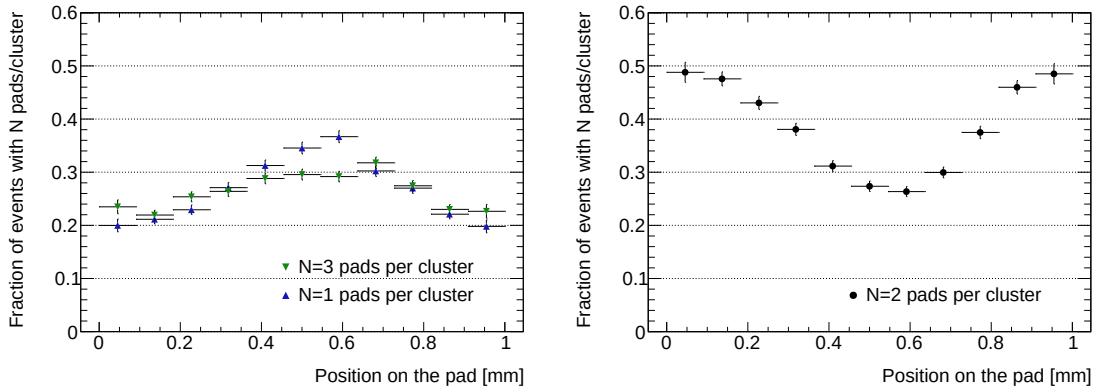

Figure 9. Fraction of events with an odd (left) or even (right) number of pads per cluster as a function of the position of the extrapolated track with respect to the pad.

2018 JINST 13 P11019

per cluster is reported as a function of the position of the extrapolated track within a pad. If the track crosses the detector in a position close to the center of a pad it will create a cluster with an odd number of pads with higher probability: if the deposited charge is low, only one pad will be fired while, if the deposited charge is high, the signal will be induced on the two adjacent pads on both sides of the fired pad. On the other hand, if the track is close to one edge of a pad, the signal will most likely be shared only between two adjacent pads.

4.2.2 Spatial resolution

The spatial residuals are here defined as the difference between the cluster position measured with the pad-MM and the position of the track reconstructed from the reference chambers and interpolated to the pad-MM. In figure 10-left the distribution of the residuals, in the precision coordinate, as measured with the high energy muon beam is reported. A residuals distribution width of 190 µm (from 1 mm pad pitch) was obtained performing a gaussian fit. In figure 10-right the residuals distribution in the second coordinate (3 mm pad pitch) is reported. This is a uniform distribution with a FWHM of about 2.4 mm and a RMS = 746 µm, that is our estimate of the residuals distribution width in the non-precision coordinate.

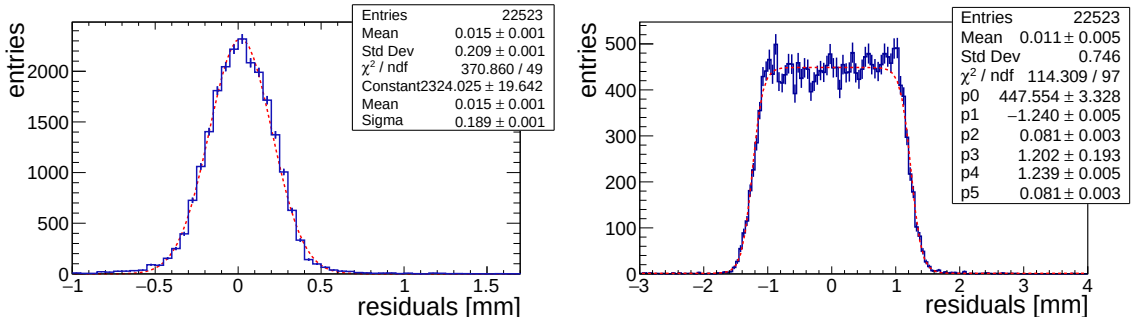

Figure 10. Residuals distribution in the precision 1 mm pitch coordinate (left) and in the second 3 mm pitch coordinate (right) as measured with an high energy muon beam for an amplification voltage of 530 V.

The spatial position resolution is derived from the residuals distribution width, after subtracting in quadrature the computed extrapolation error (50 µm) resulting from the interpolation of the reference track. As a result, the resolution will depend on the number of pads forming a cluster. In particular, as the position is measured with the charge centroid method, clusters with only one pad will have a worse resolution. As discussed in section 4.2.1 the number of pads per cluster increases with increasing amplification voltage and the fraction of clusters with one pad decreases. Thus, we expect the resolution to improve with the amplification voltage; this is shown in figure 11-left where the resolution is reported to be ∼ 210 µm at 460 V and ∼ 180 µm at 510 V and 520 V. The statistical uncertainty on the spatial resolution is negligible and the uncertainty is dominated by systematic effects. The main systematic uncertainty comes from different fit procedures of the residuals distributions: since these are not always pure single gaussians the results slightly depend on the fit function (single or double gauss function) and on the fit range. We estimated this uncertainty to be ∼ 5%.

To understand the contribution of clusters with only one pad, the resolution as measured with clusters with at least 2 pads is reported in figure 11-right; an improvement is indeed observed. The observed residual worsening of the resolution with increasing amplification voltage comes

2018 JINST 13 P11019

from the relative contribution of clusters with different number of pads and, in particular at larger amplification voltage, from charge saturation effects in the readout electronics spoiling the charge weighted centroid position. Moreover, the resolution can be affected by the higher noise at large V_{amp}, as mentioned in section 4.2.1.

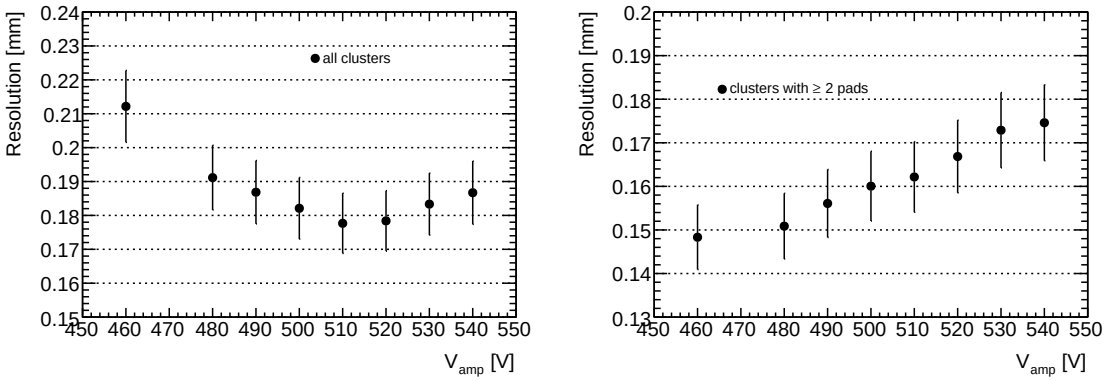

Figure 11. Spatial resolution in the precision coordinate as a function of the amplification voltage as measured with an high energy muon beam considering all the clusters (left) or only clusters with at least two pads (right). Error bars represent the evaluated systematic uncertainty, the statistical uncertainty being negligible.

4.2.3 Detector efficiency

The efficiency is measured checking, for each reference track, the presence of a cluster in the pad-MM prototype with different requirements:

1. the cluster is anywhere in the detector (cluster efficiency);
2. the cluster is within 1.5 mm of the extrapolated reference track in the precision coordinate (software efficiency);
3. the cluster is within 5σ ($\sim$ 1 mm) of the extrapolated reference track in the precision coordinate (5σ efficiency).

In figure 12 the cluster, software and 5σ efficiencies as measured with the muon beam are shown as a function of the amplification voltage. The efficiency plateau is reached at 500 V with a value larger than 99%.

5 High rate measurements

As described in section 1, we aim to a Micromegas detector with resistive pad readout for precision tracking in a high rate environment without efficiency loss up to a rate of the order of tens of MHz/cm^2. For this reason we focused our studies on the response of our prototype to a high flux of radiation. The gain has been measured as a function of the particle rate using a X-rays source and the efficiency and resolution using a high rate pion beam.

2018 JINST 13 P11019

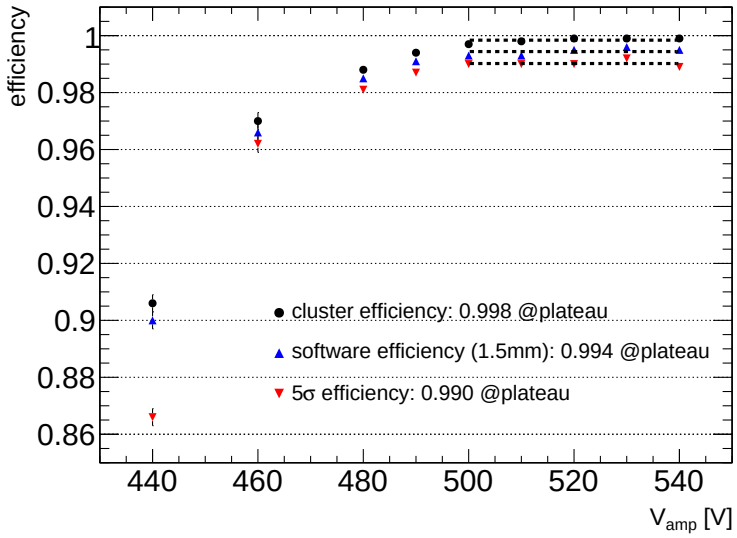

Figure 12. Detector efficiency as measured with a high energy muon beam.

5.1 Irradiation tests with X-rays

In order to measure the gain under a higher incident particle rate, the detector has been exposed to 8 keV peak energy X-rays from a Cu target. The intensity of the X-ray gun has been tuned by varying its excitation current. The photons spot has been defined using a 1 or 3 mm diameter collimator, or by shielding the detector active area with an absorber hosting a 10 mm diameter hole (see figure 13). In this way local rates of about 180 MHz/cm^2 have been reached. The schematics of the measurement setup was the same as the one described in figure 2-left. The rate has been calculated supposing that the X-rays are uniformly hitting a surface corresponding to the hole/collimator diameter: this corresponds to an underestimation of the real number of photons per square centimeter seen by the detector in the middle of the active area.

In figure 14-left the gain measured through the 10 mm hole for five different values of the amplification voltage is shown as a function of the photons rate. For this measurement a copper foil of about 70 µm was used as an attenuator of the X-rays flux. A gain reduction of about $\sim 27\%$ has been measured at 10 MHz/cm^2 photon rate for each amplification voltage value. This drop is presumably due to the charging up effect and, in a much smaller amount, to a voltage drop through the pad embedded resistors. To reach higher values of local photon rate a set of measurements has been performed removing the Cu shield and using a 3 mm collimator. Figure 14-right shows the gain measured in this condition for an amplification voltage of 530 V as a function of the photons rate, compared with the measurements at the same amplification voltage but with the 10 mm hole (already reported in figure 14-left). The amplification gain of the detector is still above 4000 up to a rate of $\sim$ 180 MHz/cm^2. In addiction, taking into account the higher ionization of the X-rays used in this measurement, the gain drop expected for the same flux of incoming MIPs is still lower.

The modulation of the gain across the small (1 mm) and large (3 mm) dimension of the pads has been measured by moving, with a step of 0.1 mm and 0.15 mm, the relative position between the detector and the 1 mm collimator of the X-ray gun along the x and y axis, respectively. Figure 15

2018 JINST 13 P11019

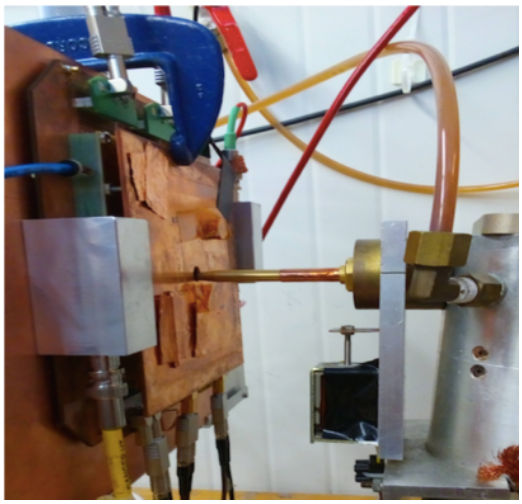

Figure 13. Picture of the detector exposed to X-rays using the 3 mm collimator

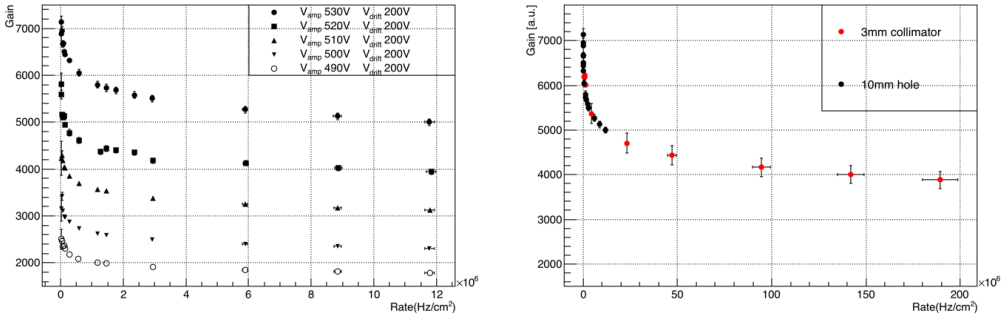

Figure 14. Detector gain as a function of ionizing radiation rate. Left: scan for different amplification voltages using the 10 mm hole [8]. Right: scan for a fixed amplification voltage (530 V) using two different collimators. Reproduced with permission from [8].

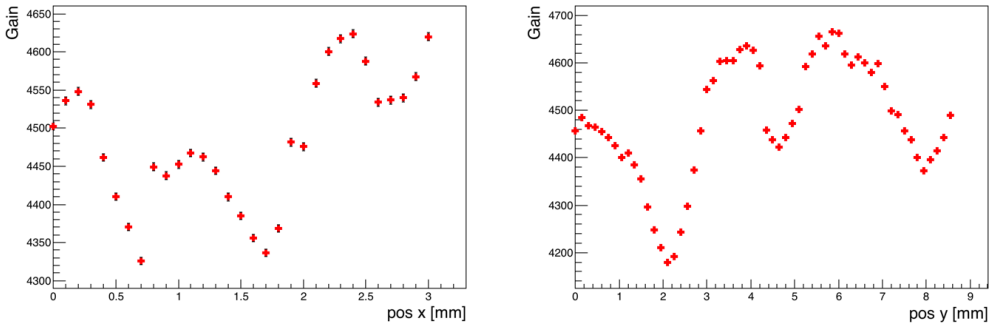

Figure 15. Gain as a function of X-rays beam position on the chamber; the 1 mm collimator has been moved by 100 µm steps in the x direction and 150 µm steps in the y direction on the detector surface. Left: scan along x position. Right: scan along y position.

2018 JINST 13 P11019

shows the results for the x and y scans, respectively, when the detector is exposed to an X-rays flux of about 3.5 MHz/cm^2. A maximum variation of the gain of a few percent, within a single pad, is observed. This modulation in gain is compatible with a non uniform electric field along the border of the resistive pads due the pattern of the dielectric/resistive material of the surface. The measured gain in the middle of each pad is different within a few percent, possibly because of the different drop in the amplification voltage for each single embedded resistor when exposed to high rate.

5.2 Measurements with a high intensity pion beam

High rates measurements with high energy charged particles have been carried out with a pion beam with the same setup described in section 4.1. Data were collected at different beam intensities with the amplification voltage fixed at 530 V and at different amplification voltages for a fixed beam intensity.

The beam rate measured by the trigger scintillator varied from 35 kHz to 400 kHz. The actual local rate per unit area is determined by the beam profile and varies on the detector surface. In figure 16 the beam profile as measured with the Tmm tracking chambers is reported in both coordinates and in the x-y plane for a run with 400 kHz trigger rate. The beam profile appears nearly gaussian with a sigma of 1.7 mm and 2.6 mm in the x and y coordinates respectively. About 20% of the events are contained in a 6 mm^2 region around the beam center (shown in the figure by the small dotted rectangle), resulting in a rate of 1.3 MHz/cm^2. On the other hand, about 1.5% of the events are contained in a region with the same surface but displaced on the external region (the solid-line rectangle in the figure), resulting in a rate of 100 kHz/cm^2. About 80% of the events are contained in a larger (49 mm^2) region around the center, resulting in a rate of 650 kHz/cm^2. It has to be noted that the lateral regions (with a much lower fraction of events) have a very small statistical impact on the measured quantities such as resolution or efficiency.

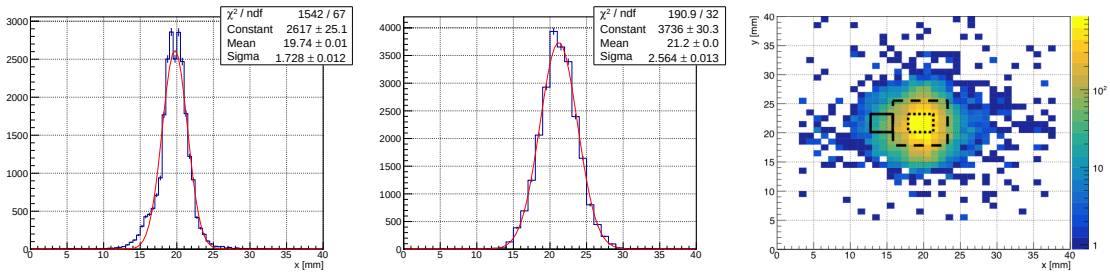

Figure 16. Pion beam profile as measured with the Tmm tracking chambers in the x (left) and y (center) coordinates and in the x-y plane (right) for a run with 400 kHz trigger rate.

The distribution of the number of clusters per event and of the number of pads per cluster reconstructed in the pad-MM have been studied as a function of the pion beam intensity. In figure 17 the two cases with lower and higher beam intensity are shown; no significant difference is observed. Neither the mean value of the number of clusters per event ($\langle N_{\text{clus}} \rangle = 1.5$) or the mean number of pads per cluster ($\langle N_{\text{pads}} \rangle = 2.5$) vary with the beam intensity; they are in good agreement with what measured with a muon beam in the same operating conditions (figures 7-right and 8-right).

2018 JINST 13 P11019

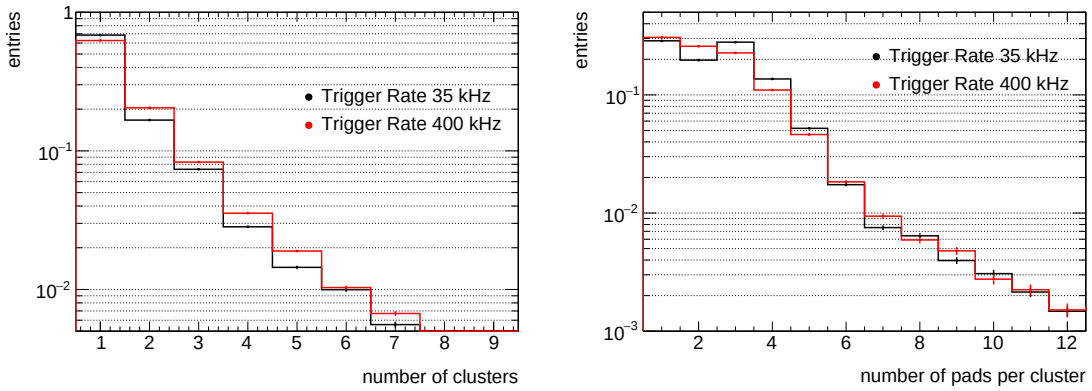

Figure 17. Distribution of the number of clusters per event (left) and of the number of pads per cluster (right) for the lowest and highest values of the trigger rate in runs with pion beam.

The pad-MM prototype spatial resolution was measured as a function of the trigger rate and the results are shown in figure 18. The resolution was computed as described in section 4.2.2 and the same comments on the systematic errors applies here. The resolution of the tracking chambers has been monitored not to change more than 15% in the runs at higher intensities; the subsequent small increase in the extrapolation error has a negligible impact on resolution measurement. We obtain a resolution of $\sim 180\,\mu$m, consistent with what measured with the low intensity muon beam in the same operating conditions (i.e. with an amplification voltage of 530 V). The small worsening of the resolution with the rate is mainly due to a slightly larger number of events in the long tails of the residuals distribution.

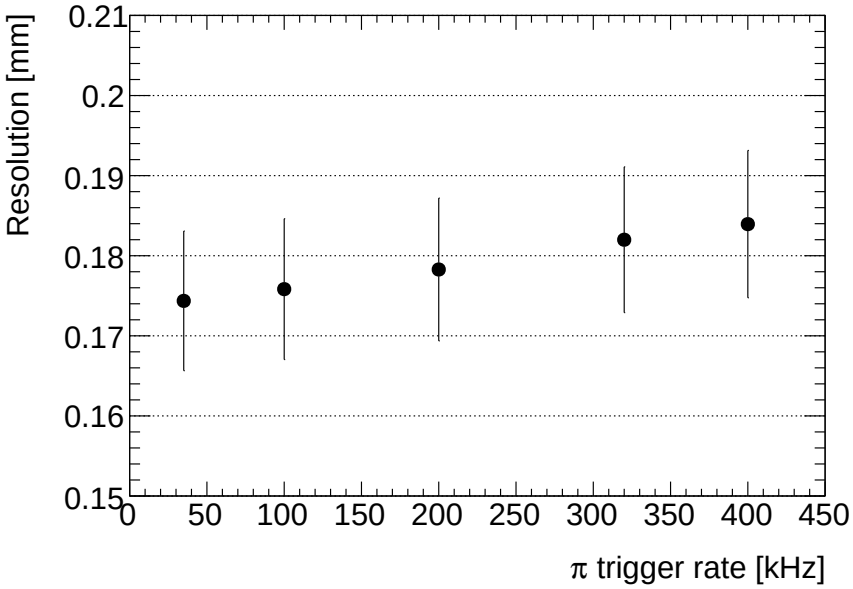

Figure 18. Detector resolution as a function of the trigger rate as measured with a high intensity pion beam. Error bars represent the evaluated systematic uncertainty, the statistical uncertainty being negligible.

2018 JINST 13 P11019

The detector efficiency was studied as a function of the trigger rate and is reported in figure 19. The details of efficiency computation and definitions can be found in section 4.2.3. The efficiency slightly drops at higher rates for tighter acceptance windows (software efficiency). If we accept clusters within 3 mm from the reference track the efficiency is constant and ~ 1; if we use the 5σ efficiency we measure a drop, but the efficiency remains larger than 98%. This means that some clusters (less than 2%) are slightly misplaced and fall out of the 5σ region. At higher beam intensities, this could be due to two particles which are close enough so that their clusters are merged, resulting in a misplacement of the centroid. The probability of two particles to be close enough to each other (~ 1 mm and ~ 2 mm in the x and y coordinates respectively) to overlap in the tracking chambers was evaluated to be about 1% at the highest beam intensity.

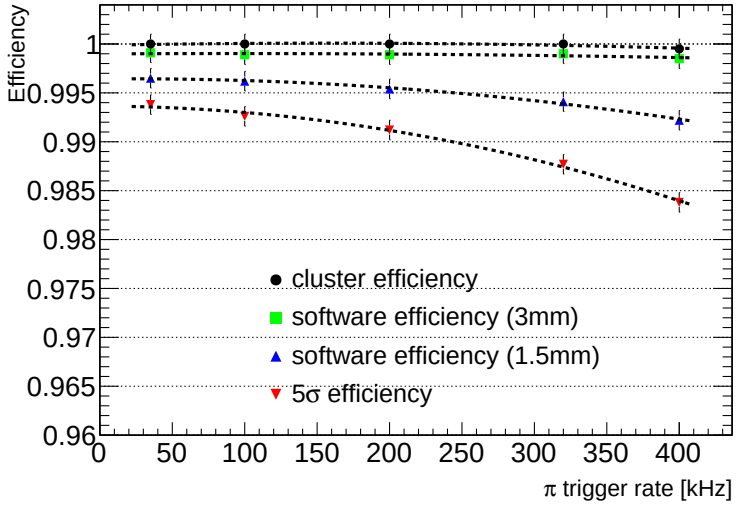

Figure 19. Detector efficiency as a function of the trigger rate as measured with a high intensity pion beam.

6 Conclusions

We have presented the design, construction technique, and test of a Micromegas with a small-pad resistive readout. The prototype has a pad pitch of 1×3 mm^2, forming a matrix with 48 pads along the precision coordinate and 16 pads along the orthogonal direction. The resistive protection is obtained with a pad-patterned resistive layer with embedded resistors connected to the anode pads.

The detector gain was measured using two ^{55}Fe sources with different activities and resulted to be larger than 5×10^3 starting at an amplification voltage of 510 V without any spark during an observation time of several hours.

The detector spatial resolution and the efficiency were measured with a high energy muon beam. In the precision coordinate, the resolution is reported to be ~ 230 µm at low amplification voltage and ~ 180 µm starting at ~ 500 V. In the non-precision coordinate, a uniform distribution with a FWHM of about 2.4 mm and a RMS = 746 µm is obtained. The efficiency plateau, as a function of the amplification voltage, shows a value larger than 99%.

2018 JINST 13 P11019

We measured both the gain as a function of the particle rate using a 8 keV peak energy X-rays gun and the efficiency and position resolution with a high rate pion beam. A gain reduction of about 20% has been measured at 10 MHz/cm^2 photon rate. At higher rates a further gain reduction, with smaller derivative, is visible; nevertheless the amplification gain of the detector is above 4000 up to a rate of 180 MHz/cm^2. The position resolution is measured not to worsen significantly with particle rate. The efficiency shows a small drop at higher beam intensity if a small acceptance window is requested (due to misplaced clusters), remaining in any case larger than 98%.

Acknowledgments

We would like to thank the CERN MPT Workshop (in particular A. Teixeira, O. Pizzirusso and B. Mehl) for the design and construction of the detector and the colleagues of the RD51 Collaboration for the support during the tests at the GDD Lab and at the H4 SPS beam line (in particular E. Oliveri and Y .Tsipolitis).

References

[1] Y. Giomataris, P. Rebourgeard, J.P. Robert and G. Charpak, *MicrOMEGAs: A High granularity position sensitive gaseous detector for high particle flux environments*, *Nucl. Instrum. Meth.* **A 376** (1996) 29.

[2] T. Alexopoulos, J. Burnens, R. de Oliveira, G. Glonti, O. Pizzirusso, V. Polychronakos et al., *A spark-resistant bulk-MicrOMEGAs chamber for high-rate applications*, *Nucl. Instrum. Meth.* **A 640** (2011) 110.

[3] ATLAS collaboration, *New Small Wheel Technical Design Report*, CERN-LHCC-2013-006 (2013).

[4] F. Thibaud et al., *Performance of large pixelised MicrOMEGAs detectors in the COMPASS environment*, 2014 *JINST* **9** C02005.

[5] M. Chefdeville, Y. Karyotakis, T. Geralis and M. Titov, *Resistive MicrOMEGAs for sampling calorimetry, a study of charge-up effects*, *Nucl. Instrum. Meth.* **A 824** (2016) 510.

[6] R. de Oliveira, *Resistive protection in MicroMegas*, talk given at the *RD51 Mini Week Workshop*, CERN, Geneva Switzerland, 22–24 February 2010.

[7] M. Alviggi et al., *Small-pads resistive MicrOMEGAs*, 2017 *JINST* **12** C03077.

[8] P. Iengo et al, *Small-pad resistive Micromegas for Operation at Very High Rates*, PoS(EPS-HEP2017)793.

[9] I. Giomataris, R. De Oliveira, S. Andriamonje, S. Aune, G. Charpak, P. Colas et al., *MicrOMEGAs in a bulk*, *Nucl. Instrum. Meth.* **A 560** (2006) 405 [physics/0501003].

[10] RD51 collaboration, *R&D Proposal Development of Micro-Pattern Gas Detector Technologies*, CERN-LHCC-2008-011 (2008).

[11] S. Martoiu, H. Muller and J. Toledo, *Front-end electronics for the Scalable Readout System of RD51*, in the proceedings of *Nuclear Science Symposium and Medical Imaging Conference (NSS/MIC)*, Valencia, Spain, 23–29 October 2011, pp. 2036–2038.

[12] M.J. French et al., *Design and results from the APV25, a deep sub-micron CMOS front-end chip for the CMS tracker*, *Nucl. Instrum. Meth.* **A 466** (2001) 359.

2018 JINST 13 P11019